Electronic Supplementary Information

A Triple Structure Design of 2D Amorphous Fe Doped Indium Phosphate Nanosheet as Highly Efficient Electrocatalysts for Water Oxidation

Jianxin Han [a], Qinghui Wei [a], Jifu Zhang [a], Bo Zhang [b], Can Li, [c,*] Wei Wang [a,d], Lixin Cao [a,*] and Bohua Dong [a,*]

[a] School of Materials Science and Engineering, Ocean University of China, 238 Songling Road, Qingdao, 266100 P. R. China

[b] School of Physical Science and Technology, Lanzhou University, 222 Tianshui South Road, Lanzhou, Gansu 730000, P.R. China

[c] Institute of Optoelectronic Materials ans Devices, College of Optical and electronic Technology, China Jiliang Unicersity

[d] Aramco Research Center Boston, Aramco Services Company, Cambridge, MA02139, USA

* Corresponding author:

E-mail: dongbohua@ouc.edu.cn; caolixin@ouc.edu.cn; canli1983@gmail.com

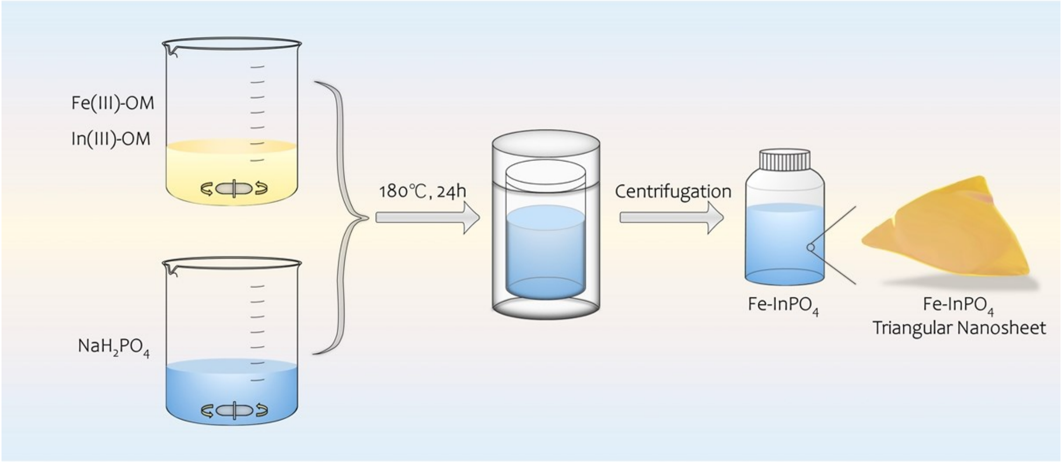

Figure S1 Synthesis illustration of of ultrathin 2D Fe-InPO$_4$ triangular nanosheets.

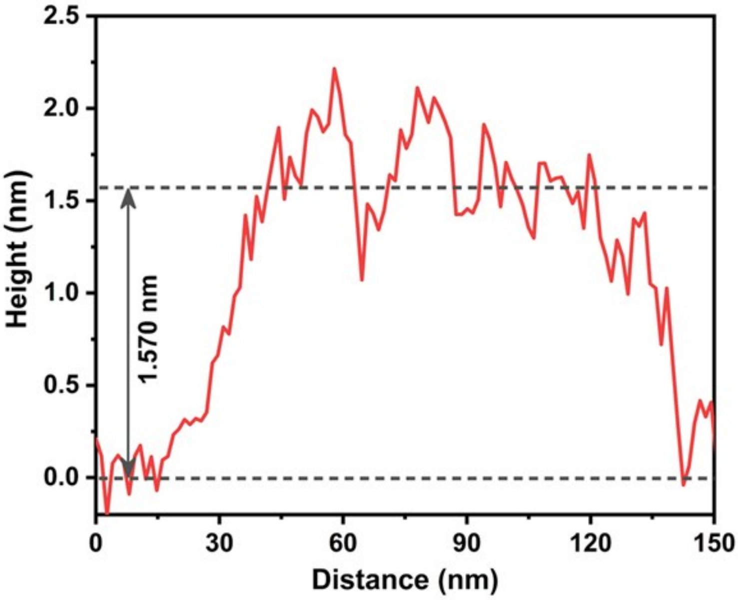

Figure S2 AFM result of Am Fe-InPO$_4$ samples.

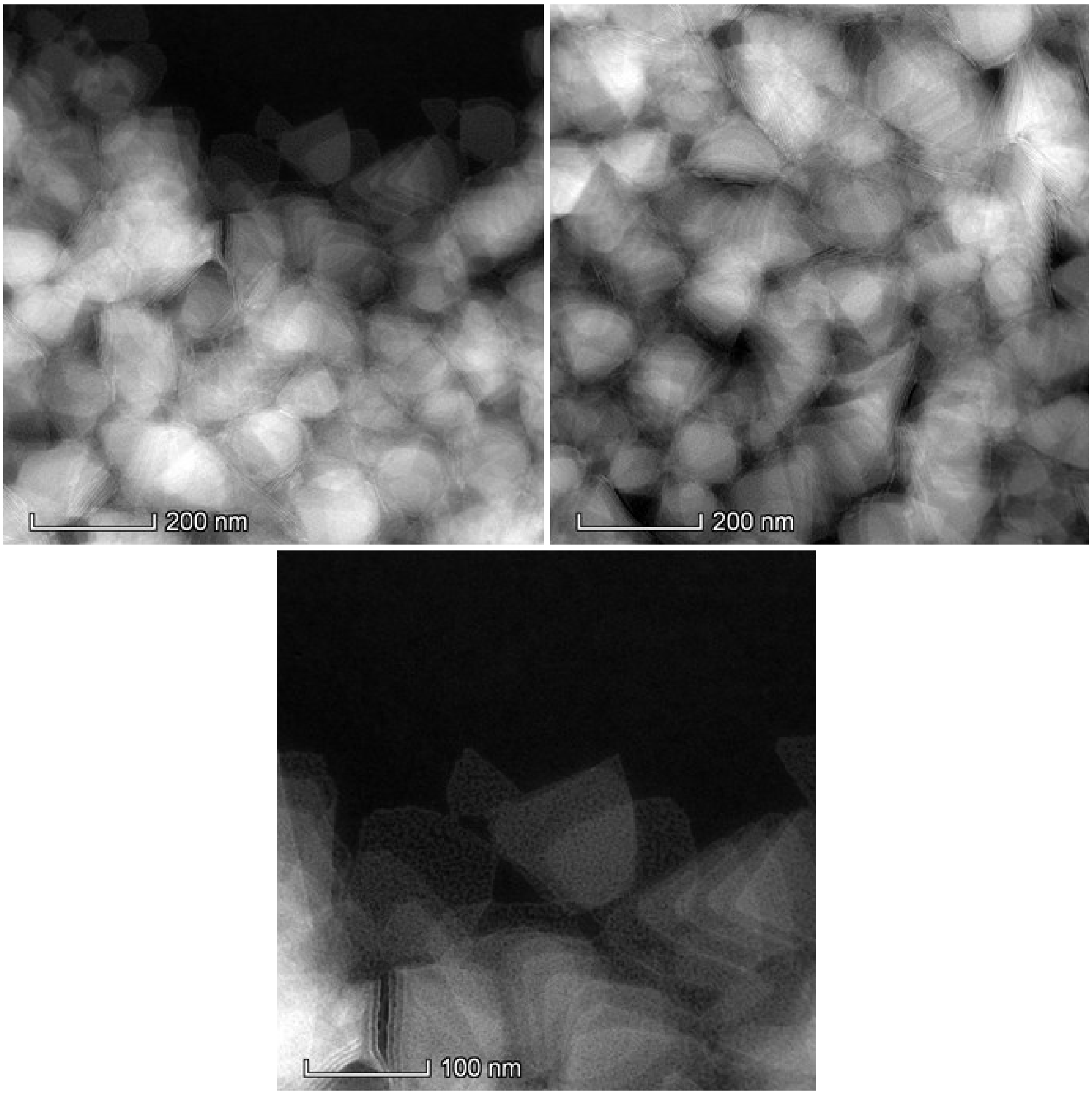

Figure S3 HADDF-STEM images of Am Fe-$InPO_4$.

Table S1 ICP-OES characterization of Am Fe-$InPO_4$ samples.

Sample	Element	CC (mg kg^{-1})
Am Fe-$InPO_4$	Fe	9760
	In	199659
	P	60192
Theoretical atomic ratio of Fe:In:P = 1:10:11		
Experimental atomic ratio of Fe:In:P = 1:9.95:11.13		

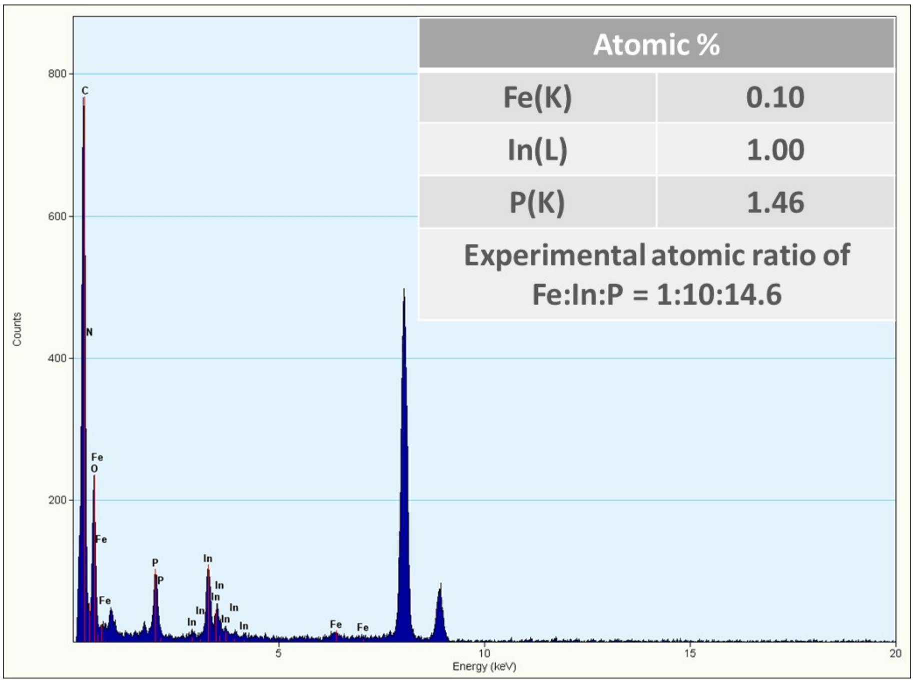

Atomic %	
Fe(K)	0.10
In(L)	1.00
P(K)	1.46
Experimental atomic ratio of Fe:In:P = 1:10:14.6	

Figure S4 EDS spectrum of Am Fe-$InPO_4$.

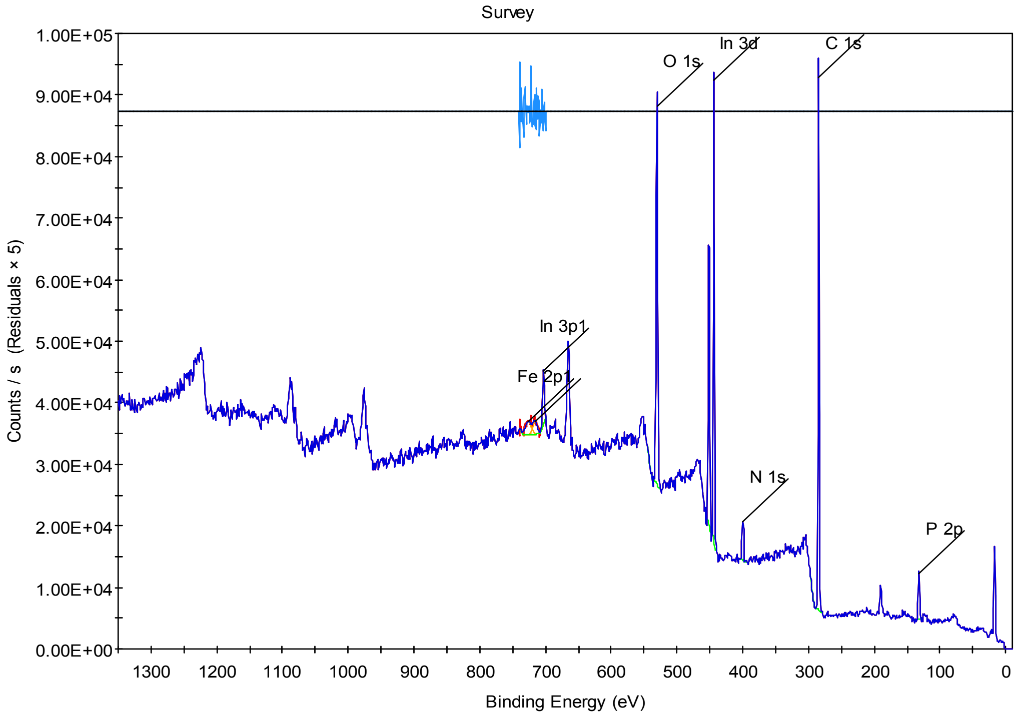

Figure S5 XPS survey of Am Fe-InPO$_4$.

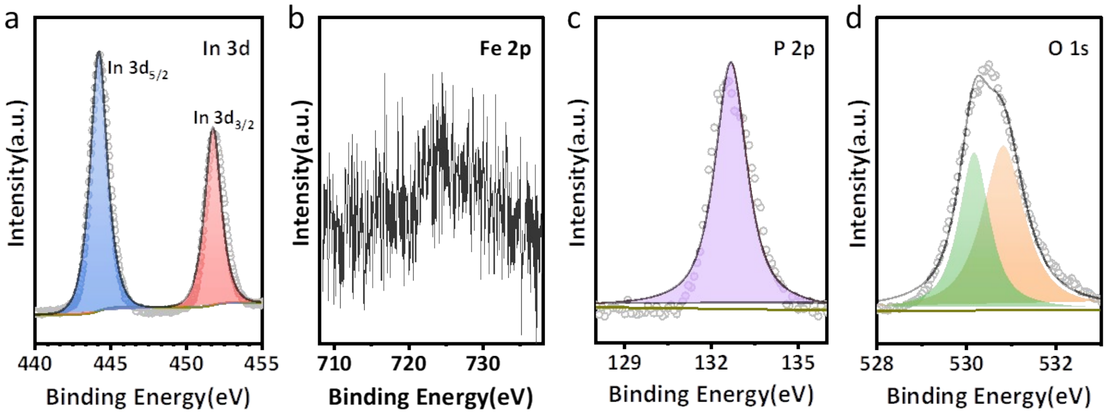

Figure S6 XPS spectra for Am Fe-InPO$_4$ of (a) In 3d, (b) Fe 2p, (c) P 2p and (d) O 1s.

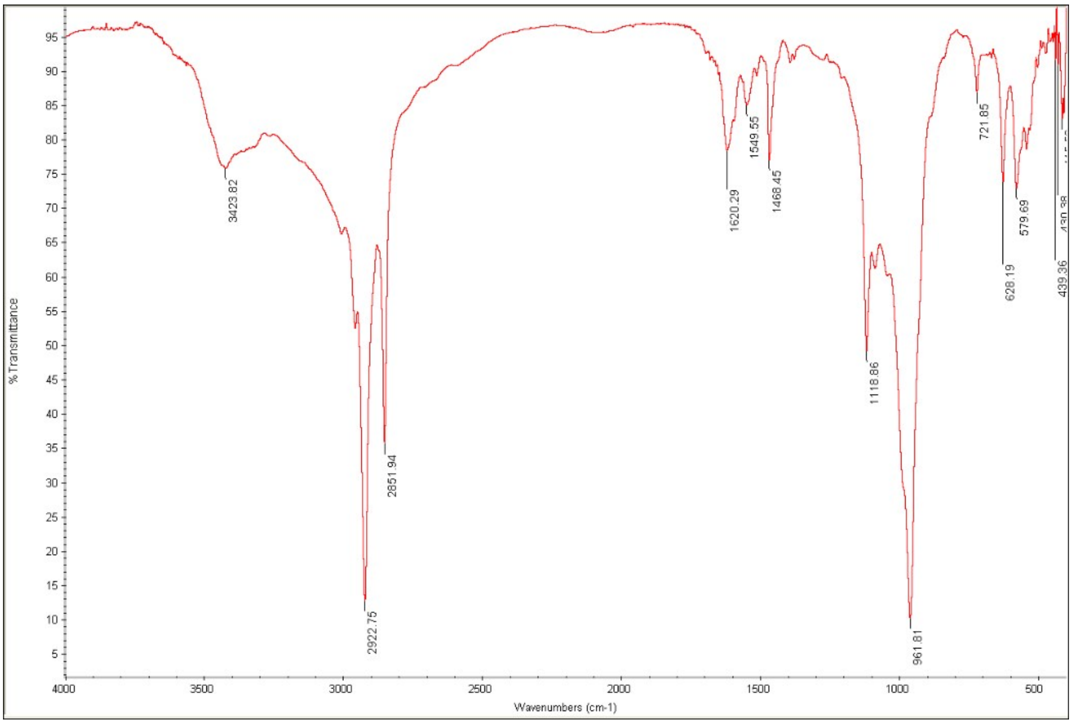

Figure S7 FTIR spectra of Am Fe-$InPO_4$.

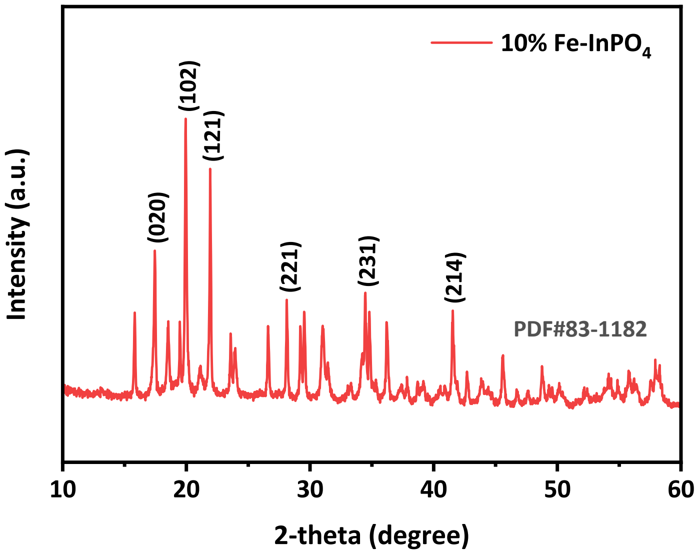

Figure S8 XRD pattern of Cr Fe-$InPO_4$ nanosheet.

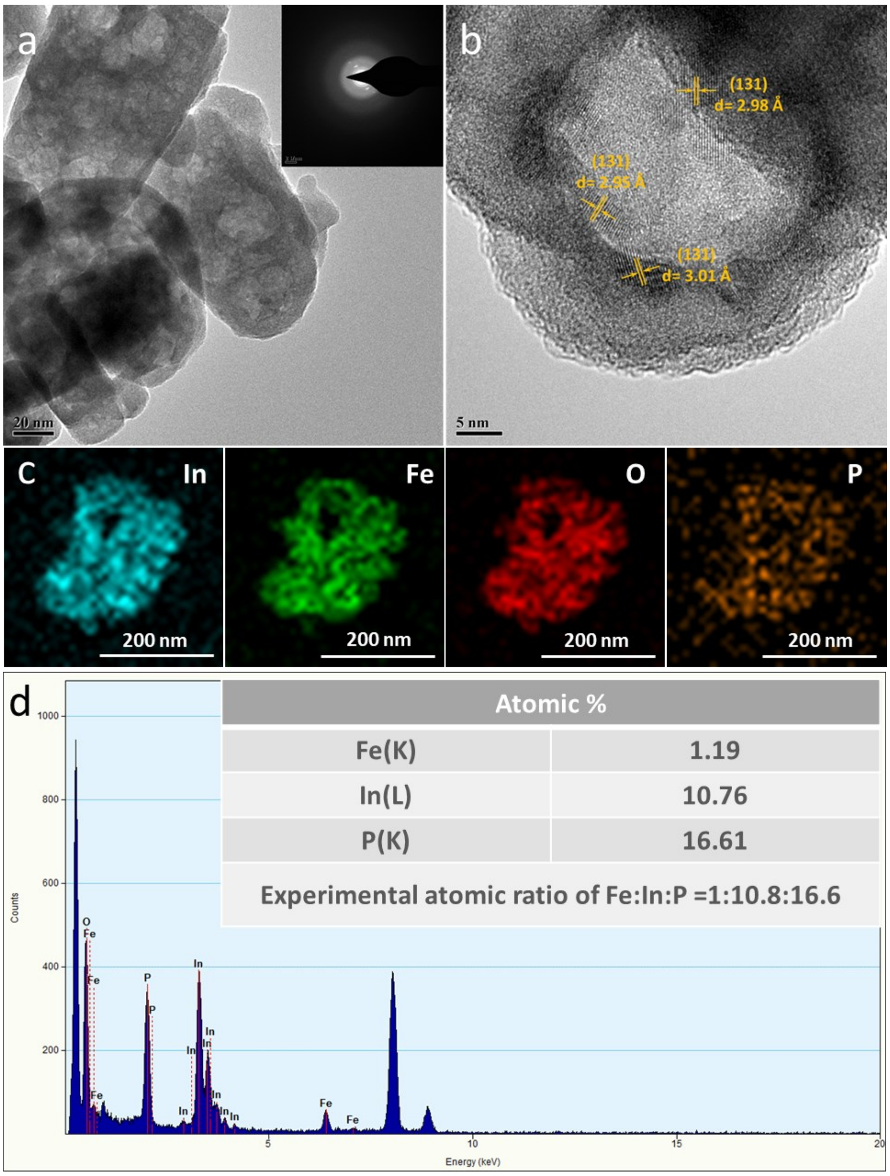

Atomic %	
Fe(K)	1.19
In(L)	10.76
P(K)	16.61

Experimental atomic ratio of Fe:In:P =1:10.8:16.6

Figure S9 (a) TEM, (b) HRTEM, (c) elemental mapping of the elements In, Fe, P and O, (d) EDS spectrum of Cr Fe-InPO$_4$.

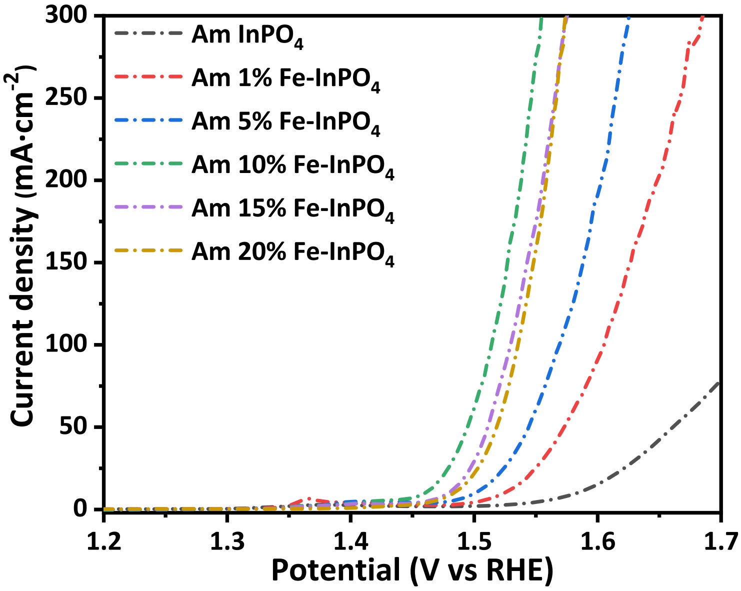

Figure S10 OER polarization curves recorded on different electrodes with a three-electrode configuration in 1.0 M KOH with 90% internal resistance (iR) compensation.

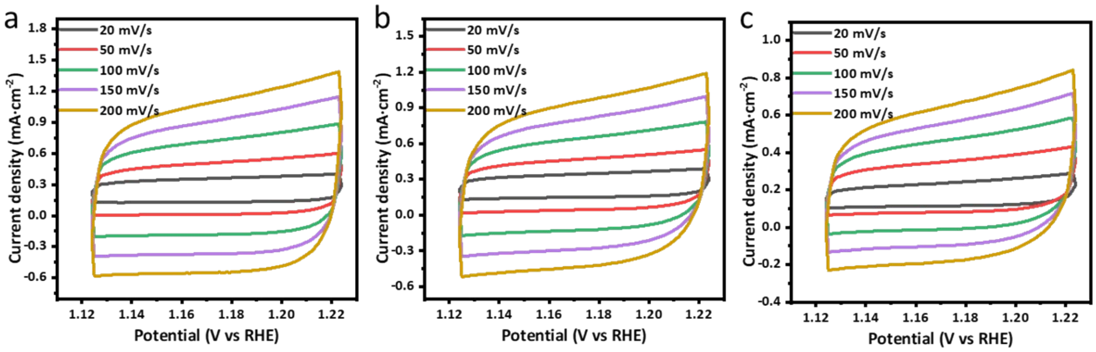

Figure S11 Cyclic voltammograms of (a) Am Fe-$InPO_4$/NF, and (b) Cr Fe-$InPO_4$/NF, and (c) Am $InPO_4$/NF.

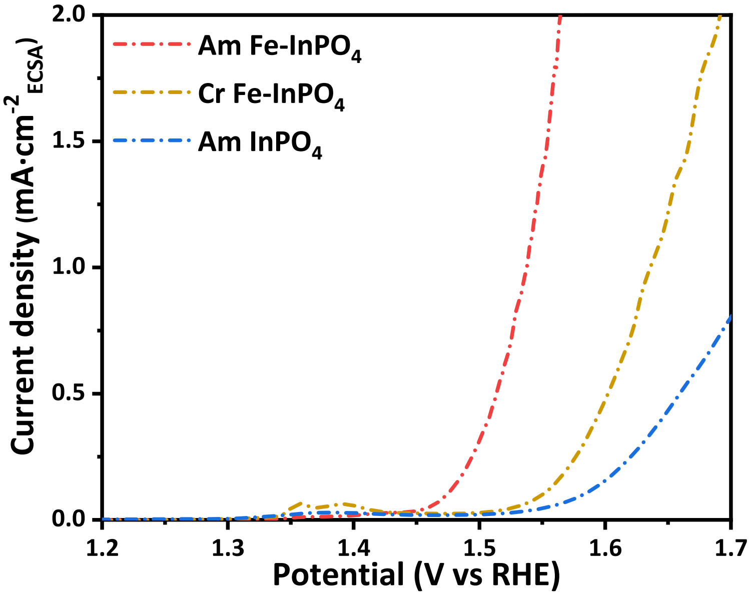

Figure S12 Normalized OER LSV curves of Am Fe-InPO$_4$/NF, Cr Fe-InPO$_4$/NF and Am InPO$_4$/NF.

The electrochemical active surface area (ECSA) is evaluated by the electrochemical double-layered capacitance (C_{dl}) according to the following equation:

$$ECSA=C_{dl}/C_s \tag{S1}$$

where C_s is the specific capacitance value of an ideal flat surface with 1.0 cm^{-2} of a real surface area. Here, C_s is 40 μF cm^{-2}.

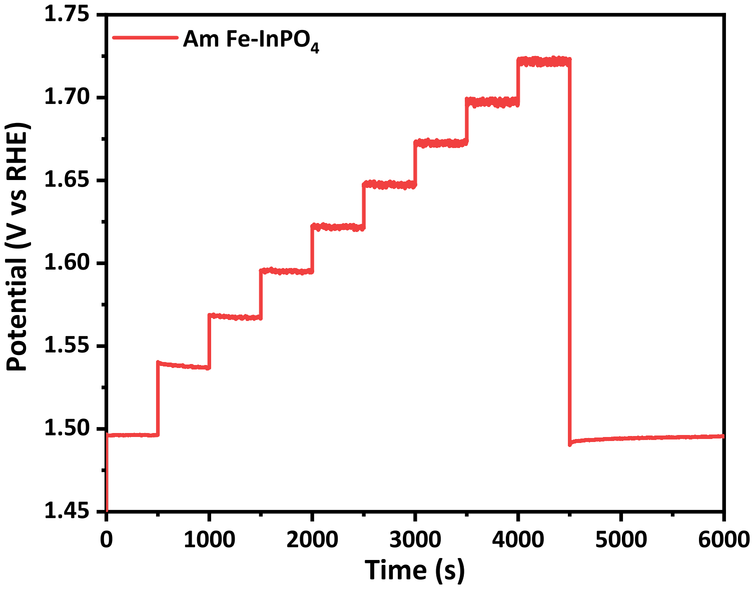

Figure S13 Multistep chronopotentiometric curve for Am Fe-InPO$_4$/NF without iR compensation.

The potential immediately levels off at 1.496 V vs RHE at the starting current value and remains unchanged for the rest of the 500 s, and the other steps also show similar results, implying excellent mass transportation and mechanical robustness of the Am Fe-InPO$_4$/NF.

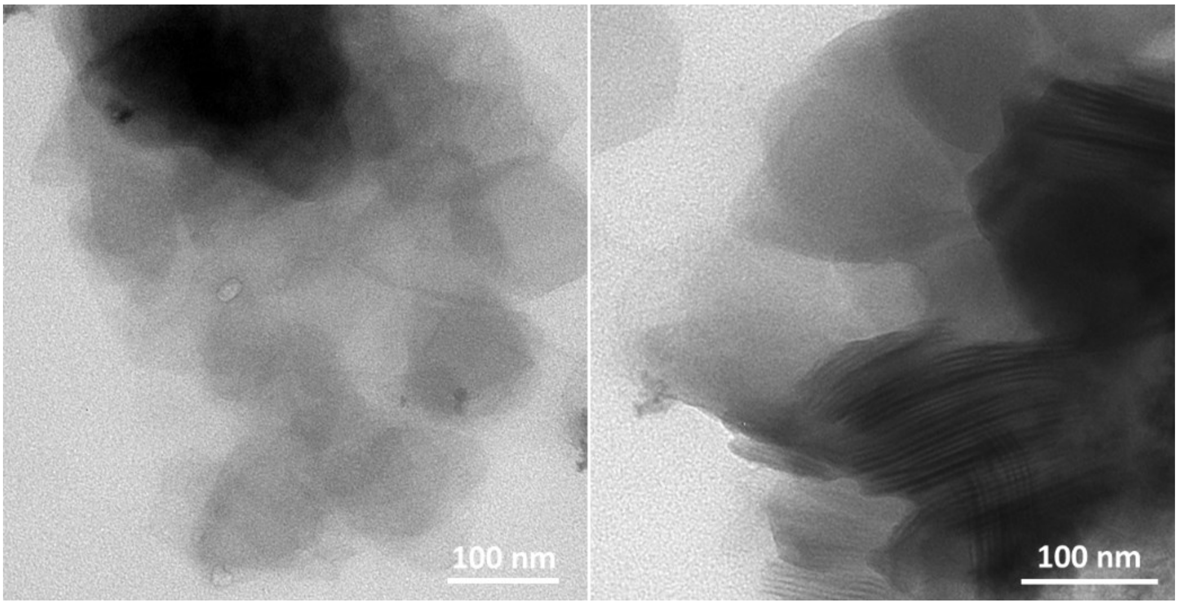

Figure S14 TEM image of Am Fe-InPO$_4$ after OER test.

Table S2 Comparison of the state-of-the-art Fe incorporated or Fe based electrocatalysts for OER in alkaline medium (j: current density; η: overpotential).

Electrocatalyst	Electrolyte	η (mV) @ j=10 mA cm^{-2}	Tafel Slope (mV dec^{-1})	Reference
Am Fe-$InPO_4$	**1.0 M KOH**	**230**	**46.47**	**This work**
FeP_x/Fe-N-C/NPC	1.0 M KOH	325	79	[1]
FeCoNi alloy	0.5 M KOH	400	72	[2]
CoFe LDH	1.0 M KOH	300	83	[3]
Fe-Ni_3C-2%	1.0 M KOH	275	62	[4]
Fe-CoP/Ti	1.0 M KOH	230	67	[5]
IPNTs	1.0 M KOH	288	43	[6]
m-NiFe/CN_x	0.1 M KOH	360	59.1	[7]
$Ni_{0.9}Fe_{0.1}$/NC	1.0 M KOH	330	45	[8]
nNiFe LDH/NGF	0.1 M KOH	337	45	[9]
$Ni_2CoFe_{0.5}$-LDH/NF	1.0 M KOH	240	65	[10]
$Ni_3V_1Fe_1$ LDH/GC	1.0 M KOH	269	68	[11]
NiFeN LDHs /GC	1.0 M KOH	280	46	[12]
$Ni_{2.5}Co_{0.5}$Fe LDHs/NF	0.1 M KOH	275	85	[13]
$CoFe_2O_4$/C NRAs	1.0 M KOH	240	45	[14]
CoFePi/$Ni(PO_3)_2$	1.0 M KOH	213	39	[15]
$Co_3(OH)_2(HPO_4)_2$	1.0 M KOH	240	69	[16]
Ni:Pi-Fe/NF	1.0 M KOH	220	37	[17]
De-LNiFeP/rGO	0.1 M KOH	270	57	[18]
NPO	0.1 M KOH	360	48	[19]
IrO_2	0.1 M KOH	360	67	[20]
RuO_2	0.1 M KOH	390	89	[20]

Method and Model:

The first principles calculations in the framework of density functional theory, including structural, electronic performances, were carried out based on the Cambridge Sequential Total Energy Package known as CASTEP.[21] The exchange–correlation functional under the generalized gradient approximation (GGA)[22] with norm-conserving pseudopotentials[23] and Perdew–Burke–Ernzerhof functional[24] was adopted to describe the electron–electron interaction. An energy cutoff of 750 eV was used and a k-point sampling set of 5 x 4 x 1 were tested to be converged. A force tolerance of 0.01 eV $Å^{-1}$, energy tolerance of 5.0×10^{-7}eV per atom and maximum displacement of 5.0×10^{-4} Å were considered. The model of crystal Fe doped InPO4 (Cr Fe-$InPO_4$) was built according to our prepared hydrated indium phosphate (PDF#83-1182), and replaced one In atom with Fe in a unit cell. The surface of Cr Fe-$InPO_4$ was cuted along the (1 0 -1) direction, and the vacuum space along the z direction was set to be 15 Å, which is enough to avoid interaction between the two neighboring images. The amorphous Fe doped $InPO_4$ model was built after relaxing Cr Fe-$InPO_4$ at 2000K, and the ordered atomic arrangement was damaged. For designing two different Fe active site in amorphous models, the coordination numbers (numbers of Fe-O bonds equal to 4 and 5 in surface models, respectively) of Fe atom were changed to adjust its electronic structure. The top three atomic layers were relaxed and the bottom three atomic layers were fixed, then the intermediates of H, OH, O, OOH groups were absorbed on the surface of substrates (see the Supporting Information for more details). Adsorption energy ΔE of A group on the surface of substrates was defined as:[25]

$$\Delta E = E_{*A} - (E_{*} + E_{A}) \qquad \text{(S2)}$$

where *A and * denote the adsorption of A group on substrates and the bare substrates, E_A denotes the energy of A group.

Gibbs free energy change (ΔG) of each chemical reaction is calculated by:

$$\Delta G = \Delta E + \Delta ZPE - T\Delta S \qquad \text{(S3)}$$

where E, ZPE, T and S denote the calculated total energy, zero point energy, temperature and entropy, respectively. Here, T = 300K is considered. The activity site of Fe was considered, the adsorption energies follow the approach of Nøeskov *et al.*,[25]

$$\Delta E_{*O} = E(\text{sub/O}) - E(\text{sub}) - [E(H_2O) - E(H_2)] \qquad \text{(S4)}$$

$$\Delta E_{*OH} = E(\text{sub/OH}) - E(\text{sub}) - [E(H_2O) - E(H_2)/2] \qquad \text{(S5)}$$

$\Delta E_{*\mathrm{OOH}} = E(\mathrm{sub/OOH}) - E(\mathrm{sub}) - [2\times E(\mathrm{H_2O}) - 3\times E(\mathrm{H_2})/2]$ (S6)

where E(sub/O), E(sub/OH) and E(sub/OOH) denote the total energies of O, OH and OOH groups on substrate. E(sub), $E(H_2O)$ and $E(H_2)$ are the total energies of bare substrate, water, and hydrogen gas, respectively.

The electrochemical model of OER developed by Nøreskov[26] can be divided into four one–electron reactions:

$H_2O + * \rightarrow {*OH} + (H^+ + e^-)$ (S7)

$*OH + (H^+ + e^-) \rightarrow {*O} + 2(H^+ + e^-)$ (S8)

$H_2O + {*O} + 2(H^+ + e^-) \rightarrow {*OOH} \quad + 3(H^+ + e^-)$ (S9)

$*OOH + 3(H^+ + e^-) \rightarrow O_2 + * + 4(H^+ + e^-)$ (S10)

The detailed Gibbs free energy changes of steps S7-S10 can be calculated by:

$\Delta G_1 = \Delta G_{*\mathrm{OH}} - eU$ (S11)

$\Delta G_2 = \Delta G_{*\mathrm{O}} - \Delta G_{*\mathrm{OH}} - eU$ (S12)

$\Delta G_3 = \Delta G_{*\mathrm{OOH}} - \Delta G_{*\mathrm{O}} - eU$ (S13)

$\Delta G_4 = 4.92\mathrm{eV} - \Delta G_{*\mathrm{OOH}} - eU$ (S14)

where the sum of $\Delta G_{1\text{-}4}$ is fixed to the negative of experimental Gibbs free energy of formation of two water molecules ($-2\Delta_{H_2O}^{exp} = 4.92$ eV).[26] The Gibbs free energy of $(H^+ + e^-)$ in solution is estimated as the half energy of H_2 molecule at standard condition.[25]

The over–potential of OER is determined by following equations:

$\eta^{\mathrm{OER}} = U_{\mathrm{OER}} - 1.23$ (S15)

$U_{\mathrm{OER}} = \mathrm{Max}\,(\Delta G_{*\mathrm{OH}}, \Delta G_{*\mathrm{O}} - \Delta G_{*\mathrm{OH}}, \Delta G_{*\mathrm{OOH}} - \Delta G_{*\mathrm{O}}, 4.92\ \mathrm{eV} - \Delta G_{*\mathrm{OOH}}) / e$ (S16)

Table S3 The calculated average bond length of Cr Fe-InPO_4 and Am Fe-InPO_4.

Average bond length (Å)	Cr Fe-InPO_4	Am Fe-InPO_4
H-O	1.023	1.015
P-O	1.531	1.533
Fe-O	1.913	1.891
In-O	2.149	2.155

The average bond lengths are calculated by Eq:

$$d_{\text{average}} = \int_{-\infty}^{+\infty} bond\ length\ *\ probability\ density\ d(bond\ length) \Big/ \int_{-\infty}^{+\infty} probability\ density\ d(bond\ length) \qquad \text{(S17)}$$

Table S4 The atomic populations of Fe species of Cr Fe-$InPO_4$ and Am Fe-$InPO_4$.

Atomic Populations of Fe species (Mulliken)							
Model	Ion	S	p	d	f	Total	Charge (e)
Cr Fe-$InPO_4$	2	0.35	0.19	6.43	0.00	6.96	1.04
Am Fe-$InPO_4$	2	0.15	0.14	6.52	0.00	6.82	1.18

Table S5 ICP-OES characterization of Am Fe (20%)-$InPO_4$ samples.

Sample	Element	CC (mg kg^{-1})
Am Fe-$InPO_4$	Fe	18830
	In	197936
	P	65668
Theoretical atomic ratio of Fe:In:P = 1:5:6		
Experimental atomic ratio of Fe:In:P = 1:5.11:6.29		

ICP-OES is used for accurately determine the Fe content of samples and the result (Table S1) indicates the content of Fe in Fe (10%)-$InPO_4$ samples cannot reach the minimum Fe mass percentage required by the Mössbauer spectrometer measurements. Thus, we use Fe (20%)-$InPO_4$ as the sample for the measurements. Table S5 gives ICP-OES result of Am Fe (20%)-$InPO_4$ and the Fe content of Am Fe (20%)-$InPO_4$ is twice that of Am Fe (10%)-$InPO_4$, which is in line with the feed ratio. We consist that the double content of Fe, as a doping element, would not have a huge impact on the analysis.

Table S6 Mössbauer parameters determined for the different iron sites of Am Fe-InPO$_4$ with 20% Fe incorporation.

	IS (mm/s)	QS (mm/s)	LW (mm/s)	RI (%)
Fe^{3+} as double	0.383	0.81	0.502	88.8
Fe^{4+} as double	-0.007	0.59	0.478	11.2

Table S7 Mössbauer parameters determined for the different iron sites of Cr Fe-InPO$_4$ with 20% Fe incorporation.

	IS (mm/s)	QS (mm/s)	LW (mm/s)	RI (%)
D1	0.46	0.31	0.43	64.6
D2	0.36	0.96	1.78	29.0
D3	0.34	0.46	0.38	6.4

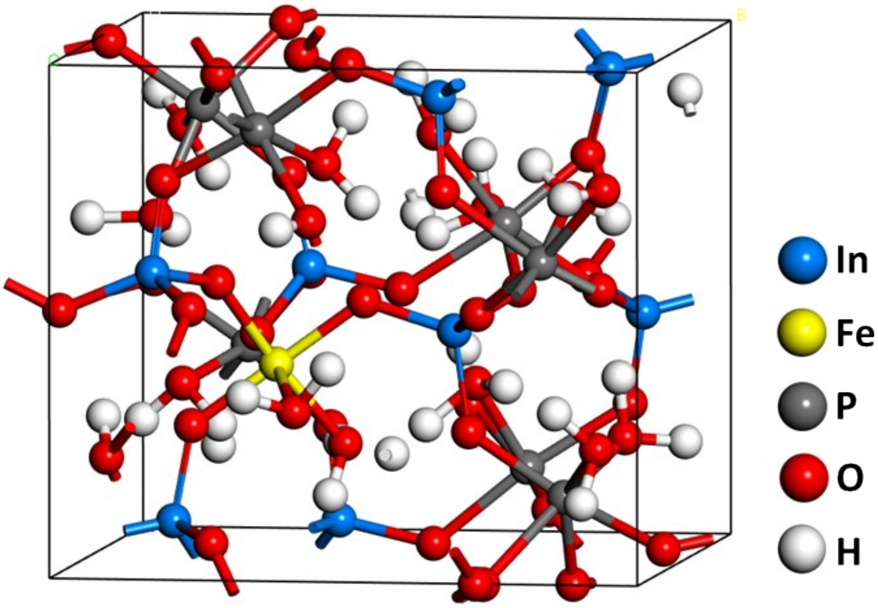

Figure S15 Model of Am Fe-2-$InPO_4$.

To study the adsorption free energy in OER process on the Fe atom with different electronic structure, two tapes of amorphous model as well as the crystal model are fabricated. For designing two different Fe active site in amorphous models, the coordination numbers (numbers of Fe-O bonds equal to 4 (Am Fe-1-$InPO_4$, which is Am Fe-$InPO_4$ in Figure 3 and above discussion) and 5 (Am Fe-2-$InPO_4$), respectively) of surface Fe active atom are changed to adjust its electronic structure.

Table S8 The atomic populations of Fe species and calculated average bond length of Am Fe-2-$InPO_4$.

<table>
<tr><th colspan="8">Atomic Populations of Fe species (Mulliken)</th></tr>
<tr><td>Model</td><td>Ion</td><td>s</td><td>p</td><td>d</td><td>f</td><td>Total</td><td>Charge (e)</td></tr>
<tr><td>Am Fe-2-$InPO_4$</td><td>2</td><td>0.19</td><td>0.14</td><td>6.43</td><td>0.00</td><td>6.76</td><td>1.24</td></tr>
<tr><th colspan="8">Average bond length (Å)</th></tr>
<tr><td colspan="2">H-O</td><td colspan="2">1.014</td><td colspan="2">Fe-O</td><td colspan="2">1.902</td></tr>
<tr><td colspan="2">P-O</td><td colspan="2">1.533</td><td colspan="2">In-O</td><td colspan="2">2.160</td></tr>
</table>

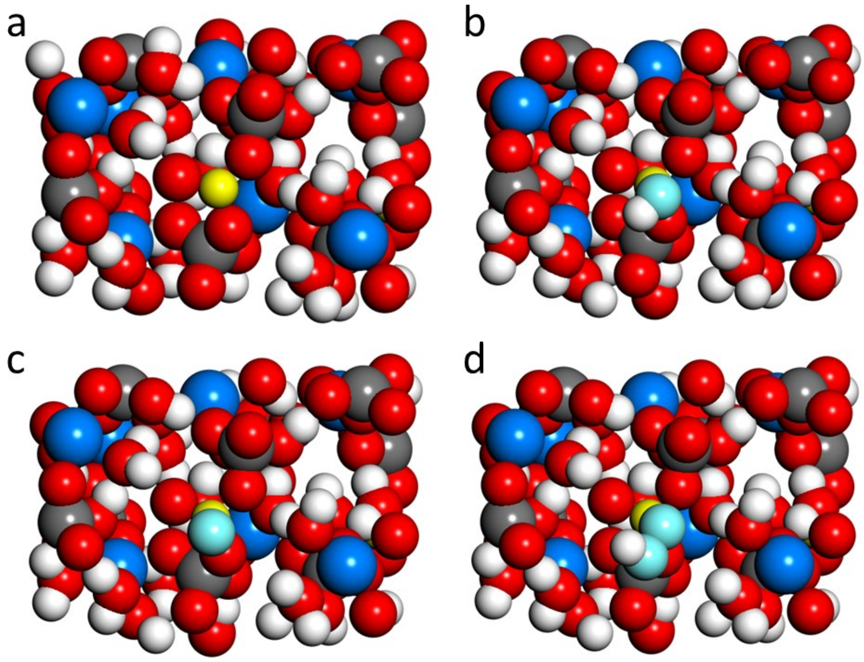

Figure S16 Optimized structures of the intermediate states in OER on surface of Cr Fe-$InPO_4$ (1 0 -1) when Fe acts as active sites (top view).

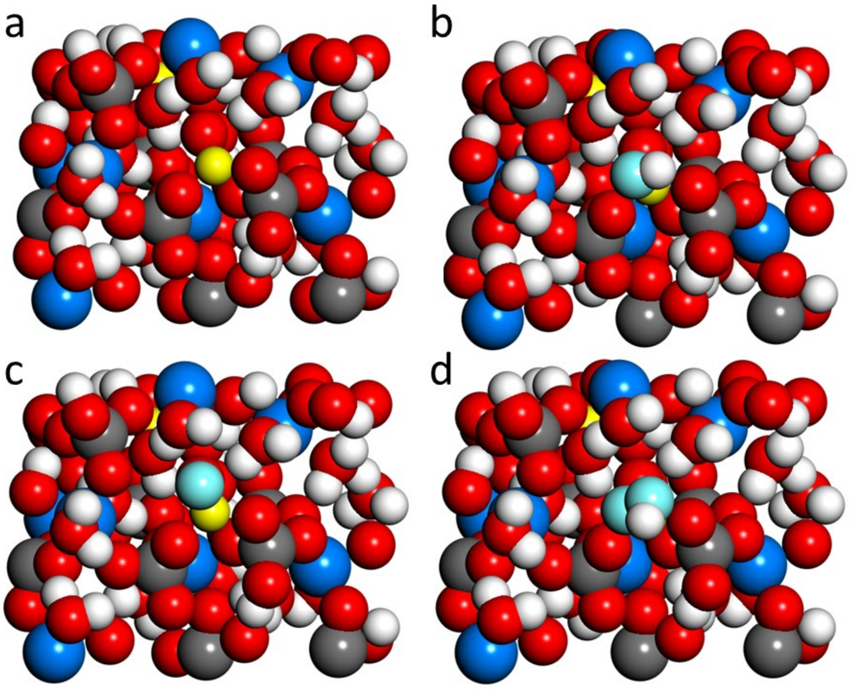

Figure S17 Optimized structures of the intermediate states in OER on surface of Am Fe-1-$InPO_4$ when Fe acts as active sites (top view).

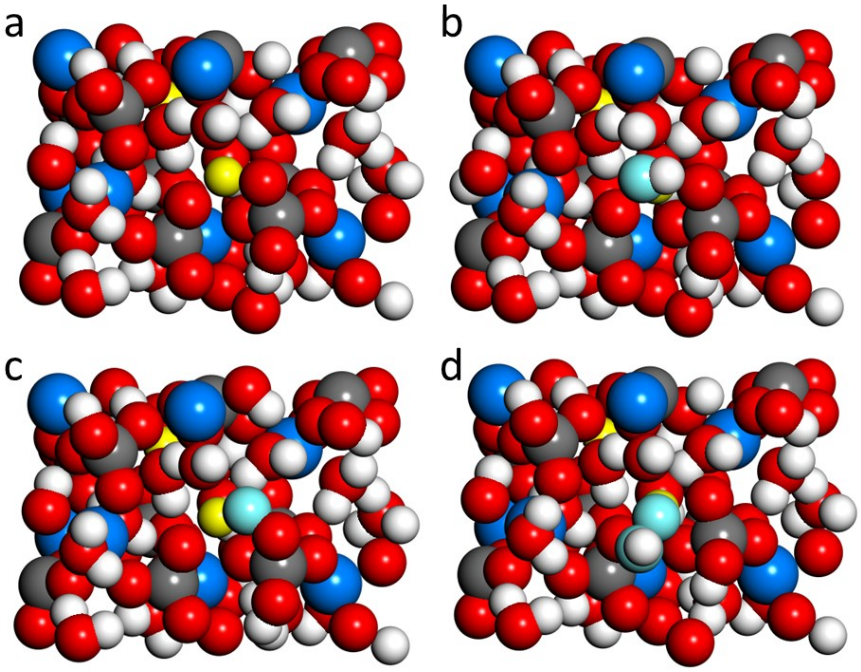

Figure S18 Optimized structures of the intermediate states in OER on surface of Am Fe-2-InPO_4 when Fe acts as active sites (top view).

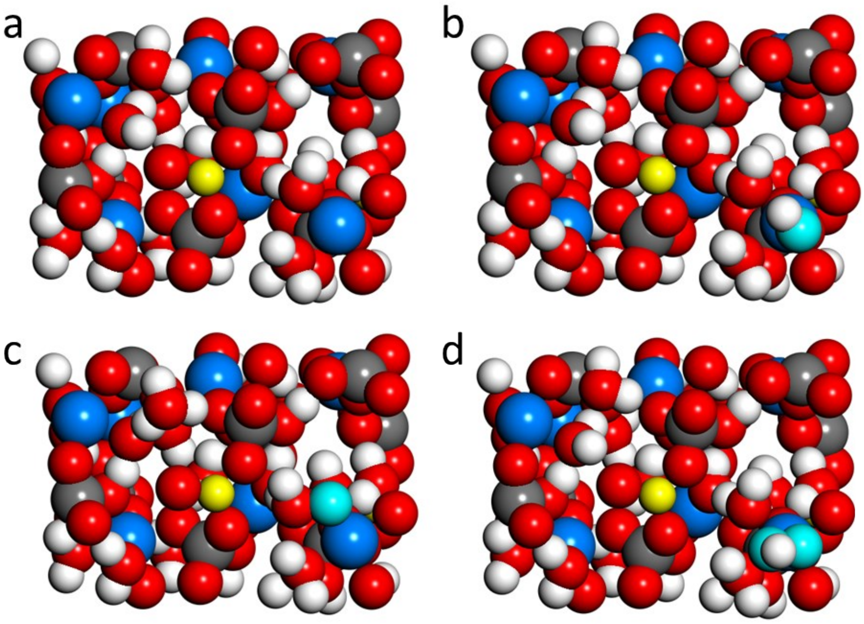

Figure S19 Optimized structures of the intermediate states in OER on surface of Cr Fe-InPO_4 when In acts as active sites (top view).

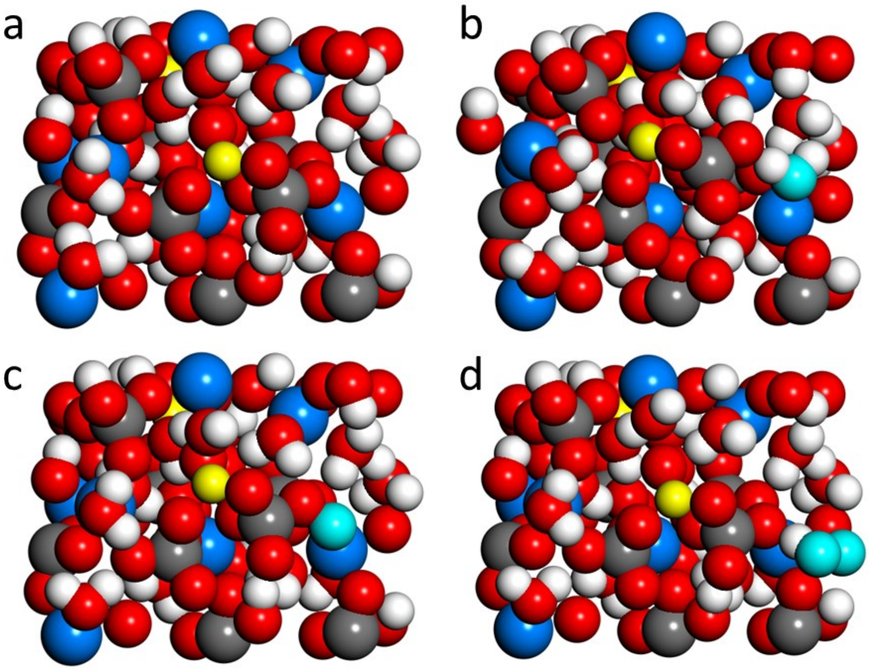

Figure S20 Optimized structures of the intermediate states in OER on surface of Am Fe-1-InPO$_4$ when In acts as active sites (top view).

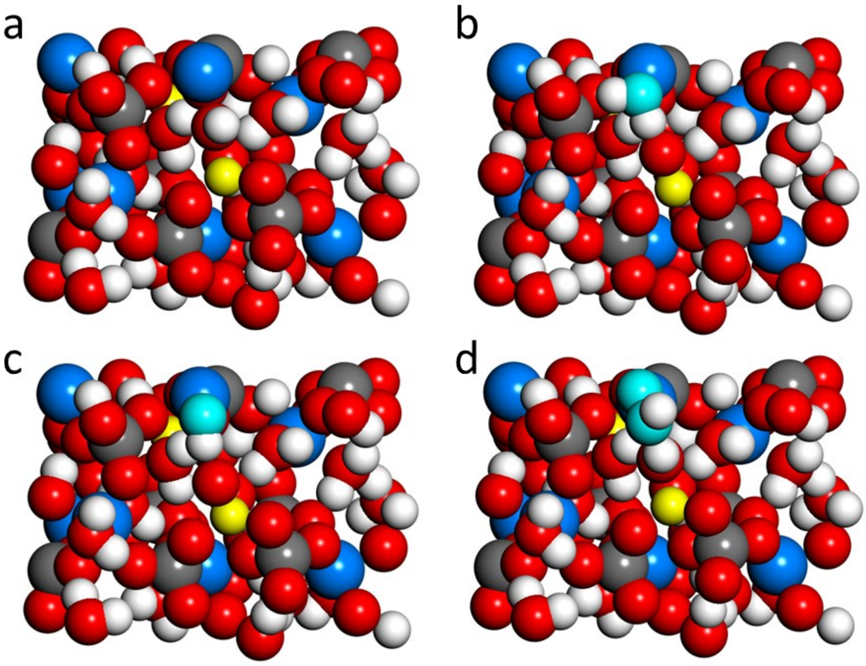

Figure S21 Optimized structures of the intermediate states in OER on surface of Am Fe-2-InPO$_4$ when In acts as active sites (top view).

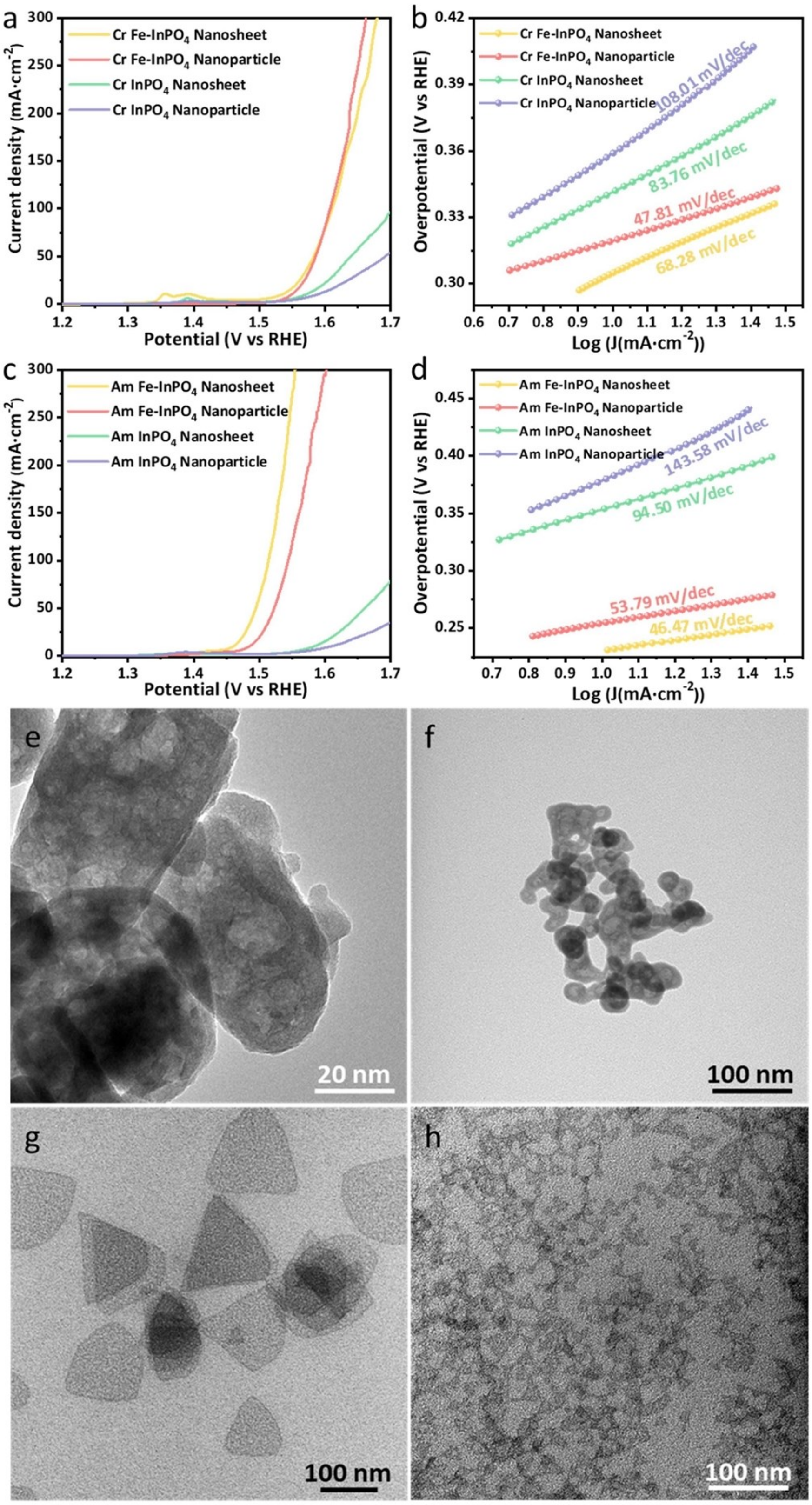

Figure S22 (a) OER polarization curves recorded on different electrodes which are shown in **Figure 5b** (left) with a three-electrode configuration in 1.0 M KOH with 90% internal resistance (iR) compensation. (b) corresponding Tafel plots for different samples of (a). (c) OER polarization curves recorded on different electrodes which are shown in **Figure 5b** (right) with a three-electrode configuration in 1.0 M KOH with 90%

internal resistance (iR) compensation. (d) corresponding Tafel plots for different samples of (c). (e) TEM image of Cr Fe-$InPO_4$ nanosheet. (f) TEM image of Cr Fe-$InPO_4$ nanoparticles. (g) TEM image of Am Fe-$InPO_4$ nanosheet. (h) TEM image of Am Fe-$InPO_4$ nanoparticles. Please note that the morphologes of undoped samples are same with that of doped samples in (e-h).

In order to investigate the structure-activity relationship between the structural features of 2D morphology, amorphization and doping of electrocatalysts, the following eight samples are taken as our research objects: crystalline 10% Fe doped $InPO_4$ nanosheet (Cr Fe-$InPO_4$ nanosheet), crystalline $InPO_4$ nanosheet (Cr $InPO_4$ nanosheet), crystalline 10%Fe doped $InPO_4$ nanoparticle (Cr Fe-$InPO_4$ nanoparticle), crystalline $InPO_4$ nanoparticle (Cr $InPO_4$ nanoparticle) and their corresponding amorphous counterparts (Am Fe-$InPO_4$ nanosheet, Am $InPO_4$ nanosheet, Am Fe-$InPO_4$ nanoparticle and Am $InPO_4$ nanoparticle). The OER performances of above electrocatalysts are shown in **Figure 5b** and **Figure S22**. As shown in **Figure 5b** (left) and **Figure S22 a-b**, both Cr $InPO_4$ nanosheet and Cr $InPO_4$ nanoparticle show greatly improved OER performance after Fe doping. In the meantime, for both Fe doped $InPO_4$ and undoped $InPO_4$, the activitys of samples with 2D morphology are better than those with 0D morphology. Based on the above results, we could predict that the sample with Fe doping and 2D morphology would exhibite the best performance towards OER among the four crystalline electrocatalysts. Actually, Cr Fe-$InPO_4$ nanosheet/NF only needs overpotential of 305 mV to afford 10 mA cm^{-2}, which meaningfully outperforms Cr $InPO_4$ nanosheet/NF (η = 342 mV for 10 mA cm^{-2}), Cr Fe-$InPO_4$ nanoparticle/NF (η = 320 mV for 10 mA cm^{-2}) and Cr $InPO_4$ nanoparticle/NF (η = 359 mV for 10 mA cm^{-2}), and the Tafel slop of Cr Fe-$InPO_4$ nanosheet/NF is also relatively small, indicating a fast reaction kinetics, which are consistent with our prediction. For the corresponding amorphous counterparts, the same laws could be revealed more distinctly from **Figure 5b** (right) and **Figure S22 c-d**, and Am Fe-$InPO_4$ nanosheet/NF shows the best OER performance. By comparing the OER performance of the crystalline samples (Figure 5b (left)) with the amorphous samples **(Figure 5b** (right)), the OER activitys of amorphous catalysts are almost better than their crystalline counterparts. As the superior catalyst with best OER performance in both crystalline catalysts and amorphous catalysts, Fe-$InPO_4$ nanosheet shows totally different activity when the crystallinity changes. Only 230 mV is required for Am Fe-$InPO_4$ nanosheet/NF to afford the current density of 10 mA cm^{-2}, which is distinctively different from that of Am Fe-$InPO_4$ nanosheet/NF, indicating the superiority of the amorphous electrocatalysts. The corresponding TEM imames of Cr Fe-$InPO_4$ nanosheet,Cr Fe-$InPO_4$ nanoparticle, Am Fe-$InPO_4$ nanosheet and Am Fe-$InPO_4$ nanoparticles are shown in **Figure S22e-h,** respectvily.

In conclusion, the structural features of 2D morphology, amorphization and doping are not indispensable. Indeed, only complementing each other, the triple structural features can simultaneously enhance the catalytic active sites and intrinsic activity of the obtained catalysts, inducing the best OER performance.

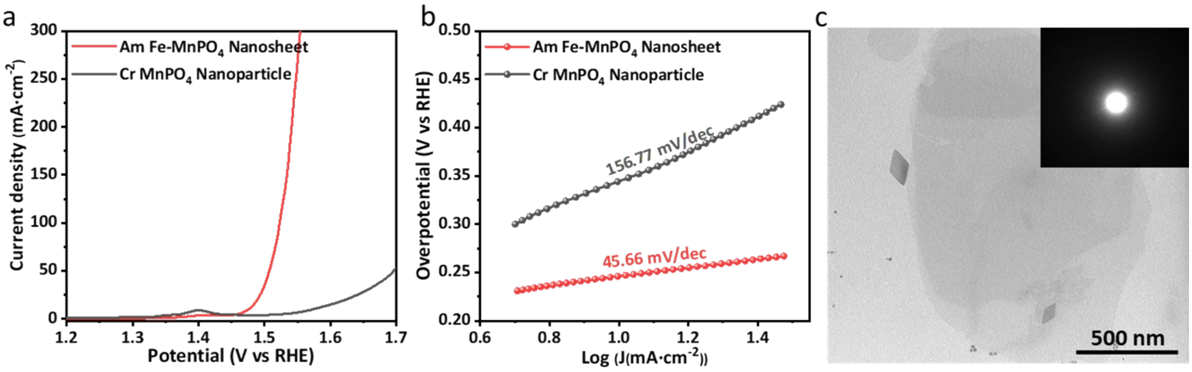

Figure S23 (a) OER polarization curves of Am Fe-$MnPO_4$ nanosheet and Cr $MnPO_4$ nanoparticle with a three-electrode configuration in 1.0 M KOH with 90% internal resistance (iR) compensation. (b) corresponding Tafel plots for Am Fe-$MnPO_4$ nanosheet and Cr $MnPO_4$ nanoparticle. (c) TEM image of Am Fe-$MnPO_4$ nanosheet.

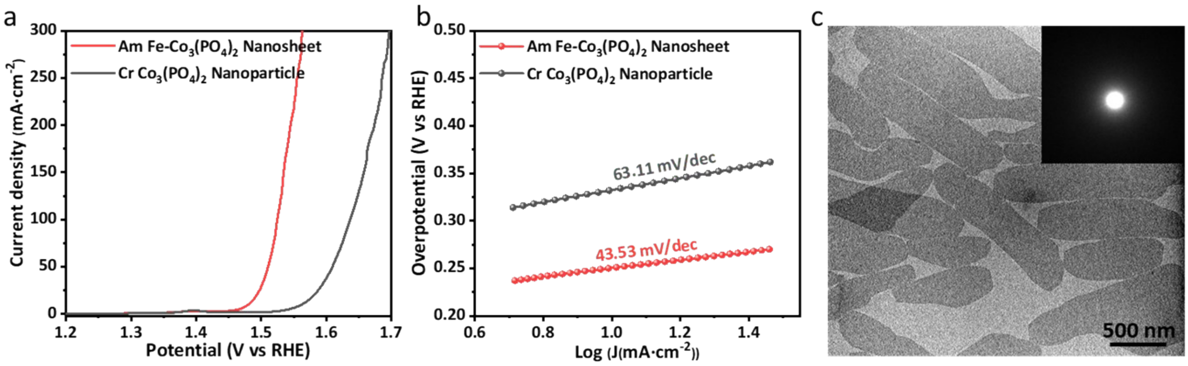

Figure S24 (a) OER polarization curves of Am Fe-Co$_3$(PO$_4$)$_2$ nanosheet and Cr Co$_3$(PO$_4$)$_2$ nanoparticle with a three-electrode configuration in 1.0 M KOH with 90% internal resistance (iR) compensation. (b) corresponding Tafel plots for Am Fe-Co$_3$(PO$_4$)$_2$ nanosheet and Cr Co$_3$(PO$_4$)$_2$ nanoparticle. (c) TEM image of Am Fe- Co$_3$(PO$_4$)$_2$ nanosheet.

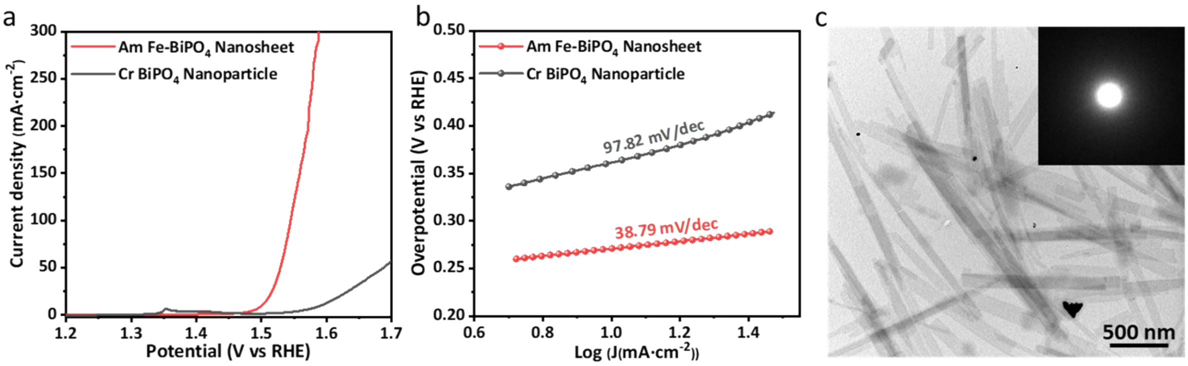

Figure S25 (a) OER polarization curves of Am Fe-BiPO$_4$ nanosheet and Cr BiPO$_4$ nanoparticle with a three-electrode configuration in 1.0 M KOH with 90% internal resistance (iR) compensation. (b) corresponding Tafel plots for Am Fe-BiPO$_4$ nanosheet and Cr BiPO$_4$ nanoparticle. (c) TEM image of Am Fe-BiPO$_4$ nanosheet.

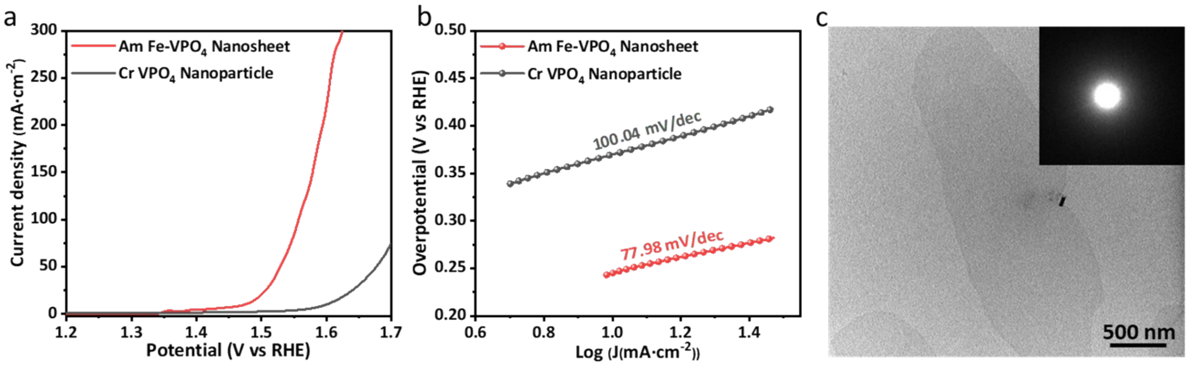

Figure S26 (a) OER polarization curves of Am Fe-VPO_4 nanosheet and Cr VPO_4 nanoparticle with a three-electrode configuration in 1.0 M KOH with 90% internal resistance (iR) compensation. (b) corresponding Tafel plots for Am Fe-VPO_4 nanosheet and Cr VPO_4 nanoparticle. (c) TEM image of Am Fe-VPO_4 nanosheet.

References

1 Q. Qin, H. Jang, P. Li, B. Yuan, X. Liu and J. Cho, *Adv. Energy Mater.*, 2019, **9**, 1803312.

2 S. Saha and A. K. Ganguli, *Chemistryselect*, 2017, **2**, 1630-1636.

3 L. Feng, A. Li, Y. Li, J. Liu, L. Wang, L. Huang, Y. Wang and X. Ge, *Chempluschem*, 2017, **82**, 483-488.

4 H. Fan, H. Yu, Y. Zhang, Y. Zheng, Y. Luo, Z. Dai, B. Li, Y. Zong and Q. Yan, *Angew. Chem., Int. Ed.*, 2017, **56**, 12566-12570.

5 C. Tang, R. Zhang, W. Lu, L. He, X. Jiang, A. M. Asiri and X. Sun, *Adv. Mater.*, 2017, **29**, 1602441.

6 Y. Yan, B. Y. Xia, X. Ge, Z. Liu, A. Fisher and X. Wang, *Chem. - Eur. J.*, 2015, **21**, 18062-18067.

7 S. Ci, S. Mao, Y. Hou, S. Cui, H. Kim, R. Ren, Z. Wen and J. Chen, *J. Mater. Chem. A*, 2015, **3**, 7986-7993.

8 X. Zhang, H. Xu, X. Li, Y. Li, T. Yang and Y. Liang, *Acs Catal.*, 2016, **6**, 580-588.

9 C. Tang, H.-S. Wang, H.-F. Wang, Q. Zhang, G.-L. Tian, J.-Q. Nie and F. Wei, *Adv. Mater.*, 2015, **27**, 4516-4522.

10 Q. Ma, B. Li, F. Huang, Q. Pang, Y. Chen and J. Z. Zhang, *Electrochim. Acta*, 2019, **317**, 684-693.

11 Z. Wang, W. Liu, Y. Hu, L. Xu, M. Guan, J. Qiu, Y. Huang, J. Bao and H. Li, *Inorg. Chem. Front.*, 2019, **6**, 1890-1896.

12 X. Jia, Y. Zhao, G. Chen, L. Shang, R. Shi, X. Kang, G. I. N. Waterhouse, L.-Z. Wu, C.-H. Tung and T. Zhang, *Adv. Energy Mater.*, 2016, **6**, 1502585.

13 X. Zhu, C. Tang, H.-F. Wang, B.-Q. Li, Q. Zhang, C. Li, C. Yang and F. Wei, *J. Mater. Chem. A*, 2016, **4**, 7245-7250.

14 X.-F. Lu, L.-F. Gu, J.-W. Wang, J.-X. Wu, P.-Q. Liao and G.-R. Li, *Adv. Mater.*, 2017, **29**, 1604437.

15 D. C. Liu, L. M. Cao, Z. M. Luo, D. C. Zhong, J. B. Tan and T. B. Lu, *J. Mater. Chem. A*, 2018, **6**, 24920-24927.

16 P. W. Menezes, C. Panda, C. Walter, M. Schwarze and M. Driess, *Adv. Funct. Mater.*, 2019, **29**, 1808632.

17 Y. B. Li and C. Zhao, *Chem. Mater.*, 2016, **28**, 5659-5666.

18 Y. Y. Liu, H. T. Wang, D. C. Lin, C. Liu, P. C. Hsu, W. Liu, W. Chen and Y. Cui, *Energy Environ. Sci.*, 2015, **8**, 1719-1724.

19 Y. Zhan, M. H. Lu, S. L. Yang, C. H. Xu, Z. L. Liu and J. Y. Lee, *Chemcatchem*, 2016, **8**, 372-379.

20 Q. Xiao, Y. Zhang, X. Guo, L. Jing, Z. Yang, Y. Xue, Y.-M. Yan and K. Sun, *Chem. Commun.*, 2014, **50**, 13019-13022.

21 M. D. Segall, P. J. D. Lindan, M. J. Probert, C. J. Pickard, P. J. Hasnip, S. J. Clark and M. C. Payne, *J. Phys.: Condens. Matter*, 2002, **14**, 2717-2744.

22 J. P. Perdew and Y. Wang, *Phys. Rev. B*, 1992, **45**, 13244-13249.

23 D. R. Hamann, M. Schlüter, and C. Chiang, *Phys. Rev. Lett.,* 1979, **43***,* 1494-1497.

24 J. P. Perdew, K. Burke and M. Ernzerhof, *Phys. Rev. Lett.*, 1996, **77**, 3865-3868.

25 Y. Wu, C. Li, W. Liu, H. Li, Y. Gong, L. Niu, X. Liu, C. Sun and S. Xu, *Nanoscale*, 2019, **11**, 5064-5071.

26 J. K. Norskov, J. Rossmeisl, A. Logadottir, L. Lindqvist, J. R. Kitchin, T. Bligaard and H. Jonsson, *J. Phys. Chem. B*, 2004, **108**, 17886-17892.